Dynamo effect in decaying helical turbulence

Axel Brandenburg,[1,2,3,4,5,*] Tina Kahniashvili,[5,6,7] Sayan Mandal,[5] Alberto Roper Pol,[1,8] Alexander G. Tevzadze,[5,7,9] and Tanmay Vachaspati[10]

[1] *Laboratory for Atmospheric and Space Physics, University of Colorado, Boulder, Colorado 80303, USA*
[2] *JILA and Department of Astrophysical and Planetary Sciences, University of Colorado, Boulder, Colorado 80303, USA*
[3] *Nordita, KTH Royal Institute of Technology and Stockholm University, Roslagstullsbacken 23, 10691 Stockholm, Sweden*
[4] *Department of Astronomy, AlbaNova University Center, Stockholm University, 10691 Stockholm, Sweden*
[5] *McWilliams Center for Cosmology and Department of Physics, Carnegie Mellon University, 5000 Forbes Ave, Pittsburgh, Pennsylvania 15213, USA*
[6] *Department of Physics, Laurentian University, Ramsey Lake Road, Sudbury, Ontario P3E 2C, Canada*
[7] *Abastumani Astrophysical Observatory, Ilia State University, 3-5 Cholokashvili Street, 0194 Tbilisi, Georgia*
[8] *Department of Aerospace Engineering Sciences, University of Colorado, Boulder, Colorado 80303, USA*
[9] *Faculty of Exact and Natural Sciences, Ivane Javakhishvili Tbilisi State University, 3 Chavchavadze Avenue, Tbilisi, 0179, Georgia*
[10] *Physics Department, Arizona State University, Tempe, Arizona 85287, USA*

(Received 4 October 2017; published 22 February 2019)

We show that in decaying hydromagnetic turbulence with initial kinetic helicity, a weak magnetic field eventually becomes fully helical. The sign of magnetic helicity is opposite to that of the kinetic helicity—regardless of whether the initial magnetic field was helical. The magnetic field undergoes inverse cascading with the magnetic energy decaying approximately like $t^{-1/2}$. This is even slower than in the fully helical case, where it decays like $t^{-2/3}$. In this parameter range, the product of magnetic energy and correlation length raised to a certain power slightly larger than unity is approximately constant. This scaling of magnetic energy persists over long timescales. At very late times and for domain sizes large enough to accommodate the growing spatial scales, we expect a crossover to the $t^{-2/3}$ decay law that is commonly observed for fully helical magnetic fields. Regardless of the presence or absence of initial kinetic helicity, the magnetic field experiences exponential growth during the first few turnover times, which is suggestive of small-scale dynamo action. Our results have applications to a wide range of experimental dynamos and astrophysical time-dependent plasmas, including primordial turbulence in the early universe.

DOI: 10.1103/PhysRevFluids.4.024608

I. INTRODUCTION

In electrically conducting fluids such as plasmas and liquid metals, steady helical turbulence is known to lead to an efficient conversion of kinetic energy into magnetic energy—a process referred to as a dynamo. Dynamos with swirling (helical) motions can be excited at relatively small magnetic Reynolds numbers, i.e., at moderate turbulent velocities and length scales, as well as moderate

*brandenb@nordita.org

electric conductivities [1,2]. This is why many dynamo experiments have employed helical flows both in the constrained and basically nonturbulent flows of the experiments performed in Riga [3,4] and Karlsruhe [5,6], as well as the unconstrained (turbulent) von Kármán flows in the experiments in Cadarache [7,8]. Many other experiments are currently being worked upon [9–12]. Their success is limited by the power that can be delivered by the propellers or pumps. A more economic type of dynamo experiment is driven by the flow that results inside a spinning torus of liquid sodium after abruptly breaking it. This leads to turbulence from the screwlike diverters inside the torus [13–15]. Theoretical studies of laminar screw dynamos have been performed [16], but the evolution of hydromagnetic turbulence is usually parameterized in ways that ignore the effects of kinetic and magnetic helicity.

The problem of magnetic field evolution in decaying helical turbulence in conducting media is far more general. Neutron stars, for example, have convective turbulence during the first minute after their formation [17,18]. The early universe could be another example of turbulence driven by expanding bubbles after a first-order phase transition [19,20]. Turbulence can also be driven by magnetic fields generated at earlier times during inflation [21,22]. Transient turbulence is also being generated as a consequence of merging galaxy clusters [23,24]. Even accretion discs may provide an example of decaying turbulence when the magnetorotational instability is not excited during certain phases [25]. A related example is that of tidal disruption events, where a star has a close encounter with a supermassive black hole and gets disrupted. During this process, tremendous shearing motion is being dissipated. A fraction of it can be dissipated magnetically via strongly time-dependent dynamo action and Joules dissipation [26]. Dynamo effects are also suspected to occur over durations of microseconds in inertial fusion confinement plasmas [27–29]. In all these cases, one deals with decaying turbulence. This is what makes the interpretation in terms of a dynamo effect complicated. Here we focus on general aspects of the dynamo mechanism rather than trying to model specific laboratory or astrophysics conditions.

In this paper, we demonstrate that in decaying helical turbulence, an initially nonhelical seed magnetic field undergoes a quasiexponential increase. In the presence of initial kinetic helicity, this growth is followed by a long ($\approx$50000 turnover times) transient decay where the magnetic energy decays like $t^{-1/2}$. This is slower than in the case of an initially fully helical magnetic field, which decays like $t^{-2/3}$. It develops inverse cascade-type behavior already well before the magnetic field becomes fully helical. To what extent the transient decay owing to initial kinetic helicity can be modeled in terms of advanced mean-field dynamo theory remains open, although potentially suitable tools such as two- and three-scale dynamo theories have been developed [30]. Previous decay simulations were always performed with strong initial magnetic fields. Only recently has the need for studying the evolution of hydromagnetic turbulence in *kinetically dominated* systems been emphasized [31]. However, no detailed study has been presented as yet, except for our own work [32], which focused on the case without kinetic helicity.

II. HELICAL DYNAMOS WITH TIME-DEPENDENT COEFFICIENTS

A simple example of a dynamo is one that works owing to the presence of kinetic helicity, $\langle \boldsymbol{\omega} \cdot \boldsymbol{u} \rangle$, where $\boldsymbol{\omega} = \nabla \times \boldsymbol{u}$ is the vorticity and $\boldsymbol{u}$ is the turbulent velocity. In stationary isotropic turbulence, a statistically averaged mean magnetic field $\overline{\boldsymbol{B}}$ obeys [1,2]

$$\partial \overline{\boldsymbol{B}}/\partial t = \nabla \times [\alpha_{\rm dyn} \overline{\boldsymbol{B}} - (\eta_{\rm t} + \eta)\mu_0 \overline{\boldsymbol{J}}], \tag{1}$$

where $\alpha_{\rm dyn} \approx -\tau \langle \boldsymbol{\omega} \cdot \boldsymbol{u} \rangle/3$ is the α effect, $\eta_{\rm t} \approx \tau \langle \boldsymbol{u}^2 \rangle/3$ is the turbulent magnetic diffusivity, η is the microphysical magnetic diffusivity, and $\overline{\boldsymbol{J}} = \nabla \times \overline{\boldsymbol{B}}/\mu_0$ is the mean current density with μ_0 being the vacuum permeability. If the coefficients are spatially constant and the domain is periodic, the solutions are eigenfunctions of the curl operator with eigenvalue k. If the coefficients were also constant in time, $|\overline{\boldsymbol{B}}|$ would be proportional to $\exp(\mathrm{i}\boldsymbol{k} \cdot \boldsymbol{x} + \gamma t)$. There would then be a growing solution that obeys $\gamma = |\alpha_{\rm dyn} k| - \eta_{\rm T} k^2$ with $\eta_{\rm T} = \eta_{\rm t} + \eta$ if $C \equiv |\alpha_{\rm dyn}|/\eta_{\rm T} k_1 > 1$, where $k_1 = 2\pi/L$ is the smallest wave number that fits into the cubic domain of size L^3.

We define the fractional helicity ϵ_{f} such that $\langle \boldsymbol{\omega} \cdot \boldsymbol{u} \rangle = \epsilon_{\mathrm{f}} \langle \boldsymbol{u}^2 \rangle / \xi_{\mathrm{K}}$, where ξ_{K} is the scale of the energy-carrying eddies, which we will later identify with the integral scale that is formally defined in terms of energy spectra. Thus, $C = \epsilon_{\mathrm{f}}/(\iota k_1 \xi_{\mathrm{K}})$, where $\iota = 1 + 3\,\mathrm{Re}_{\mathrm{M}}^{-1}$ with

$$\mathrm{Re}_{\mathrm{M}} = u_{\mathrm{rms}} \xi_{\mathrm{K}}/\eta \tag{2}$$

being the magnetic Reynolds number, $\tau = \xi_{\mathrm{K}}/u_{\mathrm{rms}}$ is the turnover time, and $u_{\mathrm{rms}} = \langle \boldsymbol{u}^2 \rangle^{1/2}$ is the rms velocity [33]. The effective wave number of the large-scale field, k_{m}, is not normally at the minimal wave number $k = k_1$, but at a larger value, so $k_1 \leqslant k_{\mathrm{m}} \leqslant (2\xi_{\mathrm{M}})^{-1}$; see, e.g., Fig. 17 of Ref. [34].

In decaying hydrodynamic turbulence, we have $u_{\mathrm{rms}}^2 \propto t^{-p}$ with exponent $p = 10/7$ if the Loitsiansky integral [35] is conserved, or $p = 6/5$ if the Saffman integral [36] is conserved. In these cases, we have $|\overline{\boldsymbol{B}}| = B_0 \exp[\int_0^t \gamma(t')\,\mathrm{d}t']$, where

$$\gamma(t) = (\epsilon_{\mathrm{f}} - \iota k_{\mathrm{m}} \xi_{\mathrm{K}}) u_{\mathrm{rms}} k_{\mathrm{m}}/3 \tag{3}$$

with $\epsilon_{\mathrm{f}} = \epsilon_{\mathrm{f}}(t)$, $\xi_{\mathrm{K}} = \xi_{\mathrm{K}}(t)$, $k_{\mathrm{m}}(t) \geqslant k_1$, and $\iota = \iota(t)$ now all being time-dependent functions. Thus, we expect a time-dependent (instantaneous) growth rate that is, to leading order, given by $u_{\mathrm{rms}}(t) k_{\mathrm{m}}(t)/3$. With these preliminary expectations in mind, let us now turn to three-dimensional turbulence simulations.

III. DYNAMOS IN DECAYING TURBULENCE

We are primarily interested in subsonic turbulence with initial Mach numbers of the order of 0.1. At those low Mach numbers, the equation of state no longer affects the flow (see Fig. 2 of the Supplemental Material to Ref. [37]) and compressibility effects are unimportant. We choose to solve for an isothermal gas where the pressure p is proportional to the local density ρ with $p = \rho c_{\mathrm{s}}^2$. This equation of state applies to the early universe where $c_{\mathrm{s}}^2 = c^2/3$, with c being the speed of light. Solving for a weakly compressible gas is computationally more efficient than solving for an incompressible fluid where the pressure is a nonlocal function of the velocity.

We neglect kinetic and two-fluid effects in our present work, which is appropriate for many astrophysical plasmas, including the early universe [38]. We thus solve the three-dimensional hydromagnetic equations

$$\frac{\partial \boldsymbol{u}}{\partial t} = -\boldsymbol{u} \cdot \boldsymbol{\nabla} \boldsymbol{u} - c_{\mathrm{s}}^2 \boldsymbol{\nabla} \ln \rho + \frac{1}{\rho}(\boldsymbol{J} \times \boldsymbol{B} + \boldsymbol{\nabla} \cdot 2\rho\nu \mathbf{S}), \tag{4}$$

$$\frac{\partial \ln \rho}{\partial t} = -\boldsymbol{u} \cdot \boldsymbol{\nabla} \ln \rho - \boldsymbol{\nabla} \cdot \boldsymbol{u}, \tag{5}$$

$$\frac{\partial \boldsymbol{A}}{\partial t} = \boldsymbol{u} \times \boldsymbol{B} - \eta \mu_0 \boldsymbol{J}, \tag{6}$$

where $\mathsf{S}_{ij} = \frac{1}{2}(u_{i,j} + u_{j,i}) - \frac{1}{3}\delta_{ij} \boldsymbol{\nabla} \cdot \boldsymbol{u}$ is the traceless rate of strain tensor, ν is the kinematic viscosity, $\boldsymbol{B} = \boldsymbol{\nabla} \times \boldsymbol{A}$ is the magnetic field, $\boldsymbol{J} = \boldsymbol{\nabla} \times \boldsymbol{B}/\mu_0$ is the current density, and μ_0 is the vacuum permeability. We consider a triply periodic domain of size L^3, so the smallest wave number in the domain is $k_1 = 2\pi/L$.

We take the initial velocity to be solenoidal and define it in Fourier space as

$$u_i(\boldsymbol{k}) = \left[\mathsf{P}_{ij}(\boldsymbol{k}) + \mathrm{i}\sigma_{\mathrm{K}} \epsilon_{ijl} \frac{k_l}{k}\right] \frac{u_0 k_0^{-3/2} g_j(\boldsymbol{k})\,(k/k_0)^{\alpha/2-1}}{[1 + (k/k_0)^{2(\alpha+5/3)}]^{1/4}}, \tag{7}$$

where $\mathsf{P}_{ij} = \delta_{ij} - k_i k_j/k^2$ is the projection operator, $\boldsymbol{g}(\boldsymbol{k})$ is the Fourier transform of a spatially δ-correlated vector field in three dimensions with Gaussian distributed fluctuations, and k_0 is wave number of the peak of the initial spectrum. It corresponds to the initial wave number of the energy-carrying eddies. We choose $k_0/k_1 = 60$. The exponent α (not to be confused with the mean-field dynamo coefficient α_{dyn}) denotes the slope of the spectrum at low wave numbers. We choose $\alpha = 4$

TABLE I. Summary of the runs discussed in this paper.

Run	σ_K	σ_M	v_{A0}/u_0	Re_M	Lu	t_e/τ_0	$q_M(t_e)$	$p_M(t_e)$
A	1	0	0.1	38–323	17 830	49 000	0.55	0.58
B	1	1	0.1	35–120	14–182	23 000	0.46	0.59
C	1	−1	0.1	37–326	29–1090	15 000	0.53	0.57
D	1	0	0.01	34–37	3–21	2500	0.38	1.10
E	1	0	0.001	30–22	0.5–4.5	400	0.35	0.70
E’	0	0	0.001	30–22	0.5–2.5	1300	0.29	0.44
F	1	0	0.1	27–21	9–17	63	0.47	1.31
G	1	0	0.1	14	3–5	26	0.29	0.50
H	1	0	0.1	8	1–6	3400	0.29	0.50

for a causally generated solenoidal field [39,40]. The fractional initial helicity is controlled by the parameter σ_K and given by $\epsilon_f = 2\sigma_K/(1+\sigma_K^2)$. For the initial magnetic field, we take the same spectrum, but with σ_M instead of σ_K, and amplitude B_0 instead of u_0. The velocity is initially fully helical ($\sigma_K = 1$) and solenoidal. We consider an initial $\boldsymbol{B}(\boldsymbol{k})$ with $\sigma_M = 0$, 1, and −1. The initial density is constant and given by ρ_0.

Viscosity ν and magnetic diffusivity η are usually very small in physical systems of interest. This is generally difficult to simulate, especially at early times if we fix ν and η to be that small. However, a self-similar evolution is made possible by allowing ν and η to be time dependent (after some time $t > t_0$; see below) with

$$\nu(t) = \nu_0 \max(t, t_0)^r, \tag{8}$$

where $r = (1-\alpha)/(3+\alpha)$ [41], which gives $r = -3/7$ for $\alpha = 4$. The time t_0 is chosen to be short ($t_0 u_{\rm rms}/\xi_M \approx 1$) but nonvanishing to prevent ν and η from becoming singular for $r < 0$. In most of the cases reported below, we assume $\eta(t) = \nu(t)/\mathrm{Pr}_M$, where $\mathrm{Pr}_M = 1$ is chosen for the magnetic Prandtl number. In some cases, we also compare with cases where $\mathrm{Pr}_M \neq 1$ and with cases where $\nu \equiv \nu_0$ and $\eta \equiv \eta_0$ are constant in time.

We define kinetic and magnetic energy spectra, $E_K(k,t)$ and $E_M(k,t)$, respectively. They are normalized such that $\int E_i(k,t)\,dk = \mathcal{E}_i$ for $i = $ K or M, where $\mathcal{E}_K = \rho_0 u_{\rm rms}^2/2$ and $\mathcal{E}_M = B_{\rm rms}^2/2\mu_0$ are the kinetic and magnetic mean energy densities and $B_{\rm rms}$ is the rms magnetic field. Time is given in units of the initial turnover time, $\tau_0 = \tau(0)$, and

$$\xi_i(t) = \int_0^\infty k^{-1} E_i(k,t)\,dk/\mathcal{E}_i(t) \tag{9}$$

is the integral scale. We have chosen $t_0/\tau_0 = 0.1$ for the time when viscosity and magnetic diffusivity become time dependent. Our runs are given in Table I, where the initial Alfvén speed $v_{A0} = B_0/\sqrt{\mu_0\rho_0}$ has been introduced and the end time of the run t_e is given. In the following, we characterize the values of ν_0 and η_0 by the time-dependent magnetic Reynolds and Lundqvist numbers,

$$\mathrm{Re}_M = u_{\rm rms}\xi_M/\eta \quad \text{and} \quad \mathrm{Lu} = B_{\rm rms}\xi_M/\eta, \tag{10}$$

respectively. Their initial and final values are indicated in Table I, respectively. Note also that we have now chosen to define Re and Re_M in terms of ξ_M instead of ξ_K. We do this because the magnetic energy spectrum has a more clearly defined peak, while that of the kinetic energy spectrum is less clear and, at least after some time, its evolution is enslaved by the magnetic field. Furthermore, we define instantaneous scaling exponents of $\mathcal{E}_i(t)$ and $\xi_i(t)$ as

$$p_i(t) = d\ln\mathcal{E}_i/d\ln t, \quad q_i(t) = d\ln\xi_i/d\ln t, \tag{11}$$

plot $p_i(t)$ versus $q_i(t)$ for $i = \mathrm{M}$ and K, and discuss the evolution of the point

$$\boldsymbol{P}_i = (p_i, q_i) \tag{12}$$

in the pq diagram. Solutions that obey invariance under rescaling [37,41,42],

$$k \to k'\ell^{-1} \quad \text{and} \quad t \to t'\ell^{1/q_i}, \tag{13}$$

all lie on the line $p_i = 2(1 - q_i)$ in this diagram.

In the case of a self-similar evolution [41,42], the magnetic energy spectra can be described by a single function $\phi(k\xi_\mathrm{M})$ of the product $k\xi_\mathrm{M}$ such that [37]

$$E_\mathrm{M}(k\xi_\mathrm{M}(t), t) \approx \xi_\mathrm{M}^{-\beta_\mathrm{M}}\phi(k\xi_\mathrm{M}), \tag{14}$$

where $\phi(k\xi_\mathrm{M})$ is a function of magnetic Reynolds and Prandtl numbers, but not of time. Note that $\xi_\mathrm{M}(t)$ varies such that the peak of the spectrum is always at $k\xi_\mathrm{M} \approx 1$. If the solutions are invariant under rescaling, they must obey $q_i = 2/(\beta_i + 3)$ [41].

By integrating $\mathcal{E}_\mathrm{M}(t) = \int E_\mathrm{M}(k, t)\,\mathrm{d}k$, one can see that

$$\mathcal{E}_\mathrm{M}(t) \propto \xi_\mathrm{M}^{-(\beta_\mathrm{M}+1)} \propto t^{-q_\mathrm{M}(\beta_\mathrm{M}+1)}, \tag{15}$$

and therefore we have $1 + \beta_\mathrm{M} = p_\mathrm{M}/q_\mathrm{M}$ [37]. On dimensional and physical grounds [43], one expects the rate of change to obey

$$\frac{d\mathcal{E}_\mathrm{M}}{dt} \propto \xi_\mathrm{M}^{-1}\mathcal{E}_\mathrm{M}^{3/2}. \tag{16}$$

Further details regarding the relation between ξ_M and $\mathcal{E}_\mathrm{M}$ depend of the conservation laws that are being obeyed. For example, when magnetic helicity is conserved, we have $\langle \boldsymbol{A} \cdot \boldsymbol{B} \rangle \propto \mathcal{E}_\mathrm{M}\xi_\mathrm{M} = \text{const}$, so $\xi_\mathrm{M} \propto \mathcal{E}_\mathrm{M}^{-1}$ and therefore $d\mathcal{E}_\mathrm{M}/dt \propto \mathcal{E}_\mathrm{M}^{5/2}$, which yields [43]

$$p_\mathrm{M} = q_\mathrm{M} = 2/3. \tag{17}$$

This, in turn, implies $\beta_\mathrm{M} = 0$, so the height of the peak of $E_\mathrm{M}(k, t)$ stays unchanged; see Eq. (14).

For our numerical simulations, we use the PENCIL CODE [44], a public code that is particularly well suited for simulating hydromagnetic turbulence. In all cases, we use 1152^3 mesh points, which are enough to ensure that the inverse-cascade effects are well reproduced; see Ref. [45] for earlier work highlighting the importance of high resolution in connection with the inverse cascade in nonhelical hydromagnetic turbulence.

IV. RESULTS

A. Kinetic and magnetic energy evolution

In Fig. 1, we plot $\mathcal{E}_\mathrm{K}(t)$ and $\mathcal{E}_\mathrm{M}(t)$ for runs A–E. $\mathcal{E}_\mathrm{M}$ is found to increase at first, reach a maximum at $t/\tau_0 \approx 10$, and then approach a late-time magnetic decay law approximately proportional to t^{-p} with $p \gtrsim 0.5$. We see that kinetic energy is transferred to magnetic energy, whose value eventually exceeds $\mathcal{E}_\mathrm{K}$. The time when this happens depends on the initial magnetic energy. For run A with $v_{\mathrm{A}0}/u_0 = 0.1$, this time is $t/\tau_0 \approx 20$ (see Fig. 1), and for run D it is $t/\tau_0 = 200$.

Although the turbulence is decaying, it is still possible to define a meaningful growth rate of the magnetic field and to estimate a critical value of the magnetic Reynolds number above which dynamo action is possible. We do this by plotting the instantaneous growth rate,

$$\gamma(t) = d\ln B_\mathrm{rms}/dt, \tag{18}$$

of the rms magnetic field B_rms. The result is shown in Fig. 2, where we plot $\gamma(t)\tau_0$ versus t/τ_0. We see that the values with the weakest initial field (i.e., in the kinematic limit) are $\gamma(t)\tau_0 \lesssim 0.5$ at early times. At later times, however, $\gamma(t)$ decreases. This is roughly consistent with Eq. (3). Furthermore, the decay is faster if η is larger, i.e., Re_M is smaller.

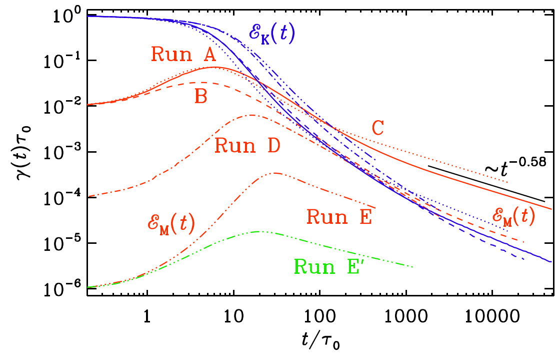

FIG. 1. Evolution of $\mathcal{E}_K$ (blue) and $\mathcal{E}_M$ (red) for $\sigma_M = 0$ (solid), $\sigma_M = 1$ (dashed), and $\sigma_M = -1$ (dotted) for $v_{A0}/u_0 = 0.1$ (runs A–C), as well as 0.01 (dot-dashed, run D) and 0.001 (triple dot-dashed, run E) for $\sigma_M = 0$. The green triple dot-dashed line denotes run E′, which has zero initial kinetic helicity.

In the case with zero kinetic helicity, the initial growth rate is nearly the same as with kinetic helicity; see run E′ in Fig. 2. This suggests that there is also small-scale dynamo action. Owing to the absence of kinetic helicity, $\gamma(t)$ follows a slightly steeper power law of the approximate form $t^{-0.9}$. At later times, however, the magnetic field of run E′ decays in the same way as that of run E.

To understand what has happened, we look at the spectra $E_K(k,t)$ and $E_M(k,t)$ in Fig. 3. We see that, during the late evolution ($t/\tau_0 > 1000$), the magnetic energy spectra are shape invariant and just translate toward smaller k. This is suggestive of an inverse cascade, where $E_M(k\xi_M(t),t)$ collapses onto the same curve $\phi(k\xi_M)$ with $1+\beta_M = p_M/q_M$ [37]; see Eq. (14). Here the correlation length ξ_M increases like t_M^q such that $\langle \boldsymbol{B}^2\rangle \xi_M^{1+\beta_M}$ stays constant; see Eq. (15). The value of this constant depends on the total amount of magnetic helicity that is *produced* in the system. To compensate for the decay in magnetic energy, we multiply E_M by $\xi_M^{\beta_M}$ with an exponent β_M such that the compensated spectra collapse onto a single function; see Fig. 4.

A closer inspection of the magnetic decay gives $q_M \approx 0.55$ and $p_M \approx 0.58$ at the end time for run A, so that $\beta_M \approx 0.05$; see the pq diagram in Fig. 5. In Fig. 6, we show a similar plot for run C. Since the magnetic decay is not truly self-similar, it does not obey the scaling relation $\beta_M = 2/q_M - 3$ [41] and does not fall on the line $p_M = 2\,(1-q_M)$, which is indicated in Fig. 5 by a solid line.

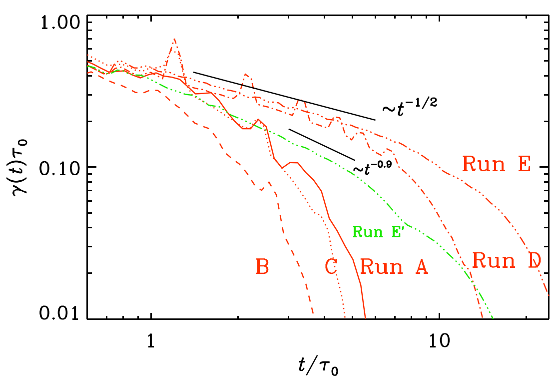

FIG. 2. Instantaneous growth rates $\gamma(t)\tau_0$ of $B_{\rm rms}$ for $\sigma_M = 0$ (solid), $\sigma_M = 1$ (dashed), and $\sigma_M = -1$ (dotted) for $v_{A0}/u_0 = 0.1$ (runs A–C), as well as 0.01 (dot-dashed, run D) and 0.001 (triple dot-dashed, run E). The green triple dot-dashed line denotes run E′ with zero initial kinetic helicity.

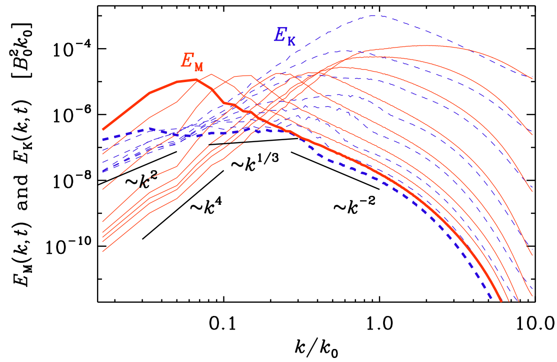

FIG. 3. $E_K(k,t)$ and $E_M(k,t)$ for $t/\tau = 16$, 60, 200, 800, 2000, 8000, and 17 000, for run A. Time is decreasing downward and the last time is shown as fat lines.

At late times, although p_M and q_M are still different from the expected law with $p_M = q_M = 2/3$, there are several other similarities to earlier calculations of magnetically dominated hydromagnetic turbulence. In particular, we see a change of the low-wave-number slope of E_K from k^4 to k^2 at later times and at small k. This is a consequence of compressibility [45,46] and is not seen in the incompressible case; see the Supplemental Material of Ref. [47]. At larger wave numbers, near the point where E_M peaks, the kinetic energy is proportional to $k^{1/3}$; see Figs. 5 and 6 and Ref. [45]. The k^2 law for the kinetic energy $\mathcal{E}_K$ is likely a consequence of turbulent interactions over the scale of the domain since the initial time.

To inspect the slow changes of $\beta_M(t)$, $p_M(t)$, and $q_M(t)$ in more detail, we show in Fig. 7 their evolution for run A using again a logarithmic time axis. We see that there is an intermediate plateau when their values are indeed approximately constant. At late times, however, we see that $\beta_M(t)$ is well described by an expression of the form $\beta_M(t) = \beta_{M0} - \beta_{M1}\ln(t/\tau_0)$. This implies that $\exp(\beta_M - \beta_{M0}) = (t/\tau_0)^{-\beta_{M1}}$. We also see that the extrapolated time t_* when $\beta_M(t_*) = 0$ is given by $t_*/\tau_0 = \exp(\beta_{M0}/\beta_{M1})$. Looking at Fig. 7 suggests that the exponents p_M and q_M both increase, although it is not obvious that they attain the value 2/3 by the extrapolated time $t_* \approx 5300$.

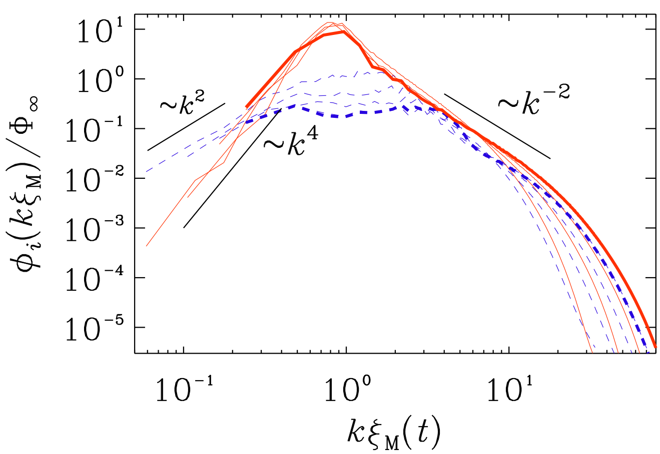

FIG. 4. $E_K(k,t)$ and $E_M(k,t)$ at $t/\tau = 2600$, 9400, 24,000, and 45,000, collapsed spectra using $\beta_M = 0$ for Run A.

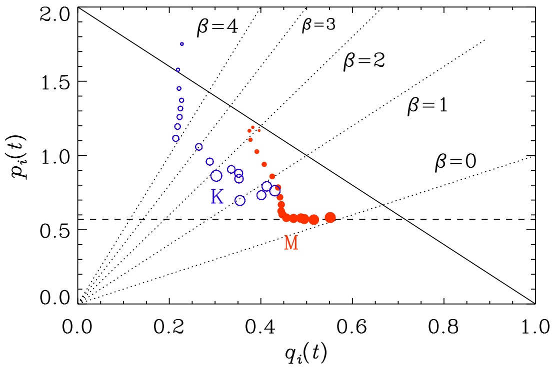

FIG. 5. *pq* diagram for run A for kinetic (blue open symbols) and magnetic (red filled symbols) energy spectra. Near the end of the run (larger symbols), the solution evolves along the $p_{\rm M} = 0.58$ line (dashed) and $q_{\rm M} \approx 0.55$ with $\beta_{\rm M} = p_{\rm M}/q_{\rm M} - 1 \approx 0.05$ is found at the end of the run. Smaller (larger) symbols denote earlier (later) times.

B. Effect of finite initial magnetic helicity

We recall that, except for runs B and C, no magnetic helicity was present initially, i.e., $\sigma_{\rm M} = 0$; see Table I. Magnetic helicity is a conserved quantity and it can only change through resistive effects and at small scales. To understand how magnetic helicity gets produced, we show in Fig. 8 magnetic and kinetic helicity spectra, $H_{\rm K}(k,t)$ and $H_{\rm M}(k,t)$, respectively. They obey the realizability conditions, $k^{-1}|H_{\rm K}(k,t)| \leqslant 2E_{\rm K}(k,t)$ and $k|H_{\rm M}(k,t)| \leqslant 2E_{\rm M}(k,t)$, respectively, and are normalized such that $\int H_{\rm K}\, dk = \langle \boldsymbol{\omega} \cdot \boldsymbol{u} \rangle$ and $\int H_{\rm M}\, dk = \langle \boldsymbol{A} \cdot \boldsymbol{B} \rangle$.

We see that, at early times, a bihelical magnetic helicity spectrum is produced, where positive and negative contributions are present simultaneously, though separated in k space, just like in driven turbulence [30,34]. Thus, there remains a near cancelation of the net magnetic helicity until the magnetic helicity spectrum saturates at $k = O(k_0)$. When that happens, magnetic helicity at large scales continues to increase only slowly such that at small scales magnetic helicity continues to dissipate resistively. Eventually, at late times, the positive magnetic helicity at small scales has disappeared and it has at all wave numbers a negative sign; see Fig. 9. Since run C starts with $\sigma_{\rm M} = -1$, we do not need to wait until the field with positive magnetic helicity gets dissipated. This leads to a more efficient transfer of kinetic energy to magnetic energy, which is why we see a stronger growth in Fig. 1. The opposite happens in the case with $\sigma_{\rm M} = 1$, where the entire spectrum

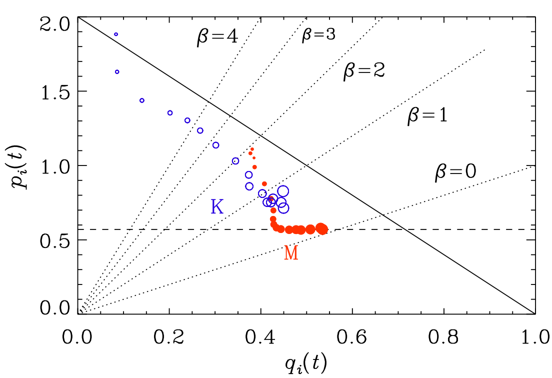

FIG. 6. Same as Fig. 5, but for run C, where the solution evolves along the $p_{\rm M} = 0.57$ line (dashed) and $q_{\rm M} \approx 0.53$ with $\beta_{\rm M} = p_{\rm M}/q_{\rm M} - 1 \approx 0.08$ is found at the end of the run.

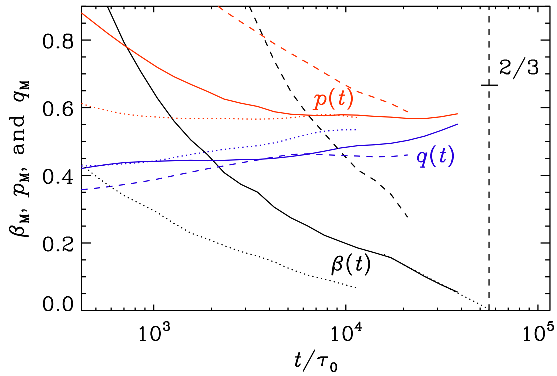

FIG. 7. Evolution of $\beta_{\rm M}(t)$ (black), $p_{\rm M}(t)$ (red), and $q_{\rm M}(t)$ (blue) for run A (solid lines), run B (dotted lines), and run C (dashed line). Note that $\beta_{\rm M}(t)$ would reach zero at an extrapolated time of $t_* \approx 5300$.

initially has the "wrong" (positive) sign, making it even harder to establish a negative magnetic helicity at all wave numbers. The total magnetic energy decays then subject to resistive decay in the presence of magnetic helicity.

C. Interpretation

In Fig. 10, we plot the evolution of $\langle \boldsymbol{B}^2 \rangle\, \xi_{\rm M}$ for different Reynolds numbers (runs A, F, and G). We see that the magnetic helicity produced depends on the magnetic Reynolds number. For comparison, we also plot $\langle \boldsymbol{B}^2 \rangle\, \xi_{\rm M}^{1.05}$ for run A. This is indicated by the dotted line, which has a flat tangent at the last time, and corresponds to $\beta_{\rm M} = 0.05$.

To make contact with the mean-field interpretation developed in Sec. II, we show in Fig. 11 that $\langle \boldsymbol{\omega} \cdot \boldsymbol{u} \rangle$ dies out while $-\langle \boldsymbol{J} \cdot \boldsymbol{B} \rangle$ increases such that $\langle \boldsymbol{\omega} \cdot \boldsymbol{u} \rangle - \langle \boldsymbol{J} \cdot \boldsymbol{B} \rangle / \rho_0 \approx$ const during the first 10 000 turnover times. It is this combination of kinetic and current helicity densities that replaces the otherwise kinematic α effect in the nonlinear regime [30,48]. At $t/\tau_0 \approx 200$, the sign of $\langle \boldsymbol{\omega} \cdot \boldsymbol{u} \rangle$ changes and has now the same sign as $\langle \boldsymbol{J} \cdot \boldsymbol{B} \rangle$. This can be explained by the strong dominance of the magnetic field over the velocity field, which begins already at $t/\tau_0 \approx 20$; see Fig. 1.

In Fig. 11, we also plot $\langle \boldsymbol{A} \cdot \boldsymbol{B} \rangle$ and see that it never reaches a constant—not even until the end of the run. This explains why $p_{\rm M}$ and $q_{\rm M}$ are still different from 2/3. By comparison with the other

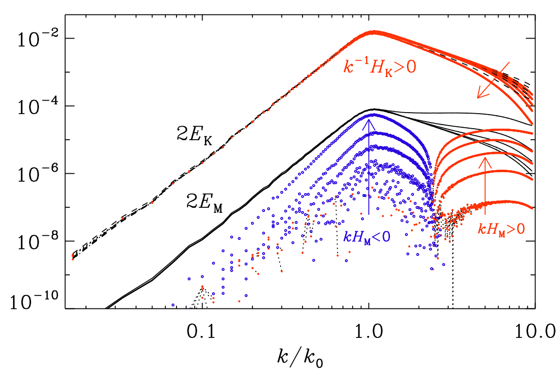

FIG. 8. $k^{-1}H_{\rm K}(k,t)$ (red) and $kH_{\rm M}(k,t)$ along with $2E_{\rm K}(k,t)$ and $2E_{\rm M}(k,t)$ (black lines) at $t/\tau = 0.05$, 0.16, 0.3, 0.6, and 1.7 for run A (red for positive values and blue for negative values). The blue and red arrows indicate the change of $kH_{\rm M}(k,t)$ with time.

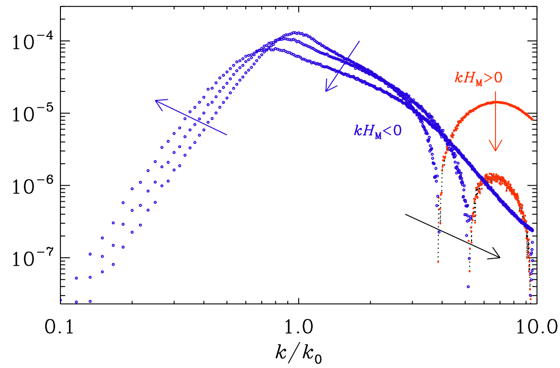

FIG. 9. $kH_M(k,t)$ (red for positive values and blue for negative values) at later times: $t/\tau = 5$, 10, and 25 for run A. The arrows indicate the temporal change of $kH_M(k,t)$.

helicities, the magnetic helicity appears to rise sharply at $t/\tau_0 \gtrsim 3 \times 10^4$ in this double-logarithmic plot. This signals the end of the $p_M \approx 1/2$ scaling of magnetic energy and the beginning of a $t^{-2/3}$ scaling after even later times.

We emphasize that in Fig. 11 we have plotted the time axis logarithmically and have normalized by the time-varying rms velocity. In this way, we were able to display the various sign changes of kinetic and current helicities, but it has also distorted the view. For this reason, we show in Fig. 12 in separate panels the kinetic, current, and magnetic helicities with a constant normalization using the initial velocity and the initial peak wave number in Figs. 12(a)–12(c) along with time-dependent normalizations using the wave number of the domain k_1 in Figs. 12(d)–12(f), with a linear time axis for the magnetic helicity in Fig. 12(f). We see that magnetic helicity is always negative, reaches a peak at $t/\tau_0 = 10$, and then decays, before asymptoting to a finite value. When normalized by $u_{\rm rms}^2$, the modulus of the magnetic energy increases approximately linearly; see Fig. 12(f).

The current helicity normalized by $u_{\rm rms}^2$ shows a negative peak at $t/\tau_0 \approx 1000$. This is when $\langle \boldsymbol{\omega} \cdot \boldsymbol{u} \rangle$ reached a negative peak, confirming again that the reason for its sign change is indeed related to the current helicity, which is then also negative and much stronger than the kinetic helicity.

D. Robustness of the $t^{1/2}$ scaling

It is here for the first time that the $t^{1/2}$ scaling has been observed. Several potentially important assumptions have been made and it needs to be seen to what extent they might affect our findings.

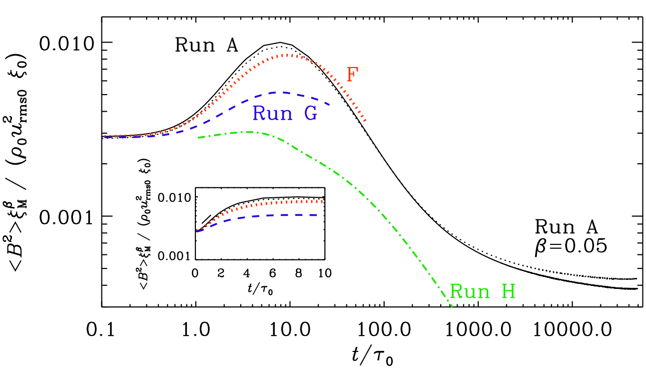

FIG. 10. Evolution of $\langle \boldsymbol{B}^2 \rangle \xi_M^\beta$ with $\beta = 0$ for run A (black solid), F (red dotted), G (blue dashed), and H (green dash-dotted). In fully helical turbulence, we expect $\langle \boldsymbol{B}^2 \rangle \xi_M \to$ const, but here $\langle \boldsymbol{B}^2 \rangle \xi_M^{1+\beta_M} \approx$ const with $\beta_M = 0.05$ at the end of the run.

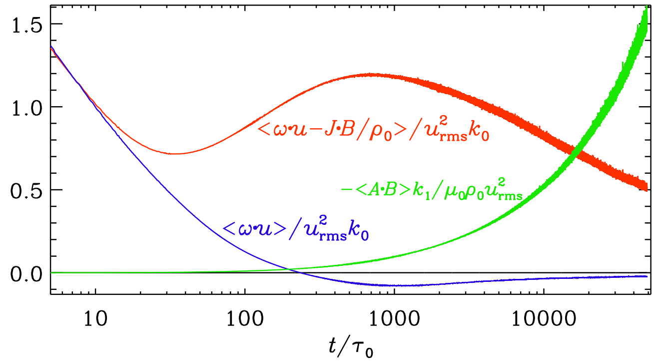

FIG. 11. Evolution of $\langle\boldsymbol{\omega}\cdot\boldsymbol{u}\rangle$ (blue), $\langle\boldsymbol{\omega}\cdot\boldsymbol{u}-\boldsymbol{J}\cdot\boldsymbol{B}/\rho_0\rangle$ (red), and $\langle\boldsymbol{A}\cdot\boldsymbol{B}\rangle$ (green) for Re = 160 (run A).

Here we examine both the assumption of using $\mathrm{Pr_M}=1$ and the assumption of using a time-dependent viscosity and a time-dependent magnetic diffusivity. In Figs. 13(a) and 13(b), we plot the results for $\mathrm{Pr_M}=0.1$ and 10, respectively. In both cases, a similar evolution of $(p_\mathrm{M},q_\mathrm{M})$ along the line $p_\mathrm{M}\approx 1/2$ is seen while q_M increases and approaches the $p_\mathrm{M}=2(1-q_\mathrm{M})$ line. Reaching this point would require a larger dynamical range and thus much larger domains and computation times than what has been possible so far. This is because, in the present runs, $k_1\xi_\mathrm{M}$ becomes rather small ($\lesssim$3) toward the end of the run, so inverse transfer is no longer independent of the system size.

In Fig. 13(b), we also see that the trajectory overshoots the $p_\mathrm{M}\approx 1/2$ line when $\mathrm{Pr_M}=10$. This overshooting indicates that η is still too small for our numerical resolution of 1152^3 mesh points. We have seen a similar behavior also when using a time independent but very small value of $\nu=\nu_0$; see Fig. 14 for such an example.

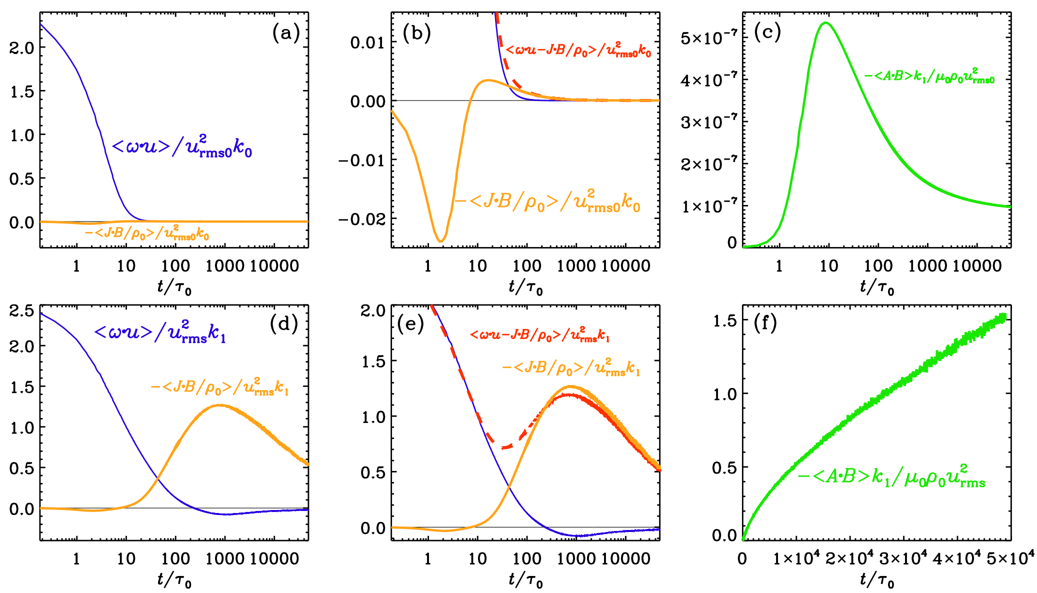

FIG. 12. Similar to Fig. 11, but with different normalizations, using in panels (a)–(c) the initial velocity and the initial peak wave number, in panels (d)–(f) the time-dependent velocity using k_1, with a linear time axis for magnetic helicity in panel (f) in separate panels focusing on $\langle\boldsymbol{\omega}\cdot\boldsymbol{u}\rangle$ (blue), $\langle\boldsymbol{\omega}\cdot\boldsymbol{u}-\boldsymbol{J}\cdot\boldsymbol{B}/\rho_0\rangle$ (red), $-\langle-\boldsymbol{J}\cdot\boldsymbol{B}/\rho_0\rangle$ (orange), and $\langle\boldsymbol{A}\cdot\boldsymbol{B}\rangle$ (green) for Re = 160 (run A).

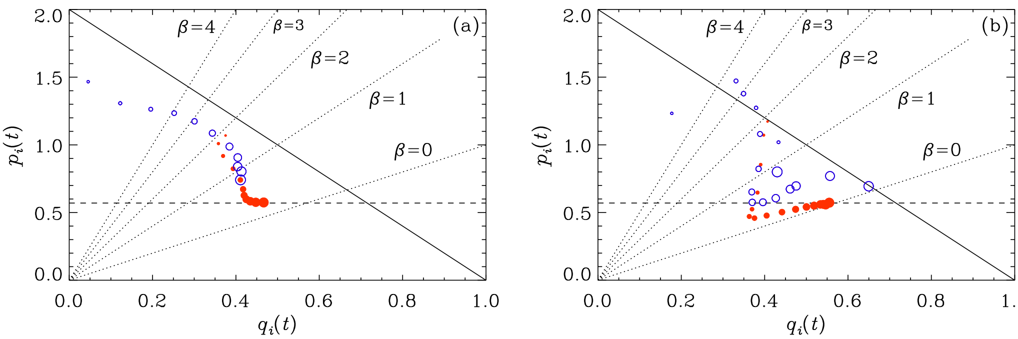

FIG. 13. *pq* diagram for $\mathrm{Pr_M} = 0.1$ (a) and 10 (b). Smaller (larger) symbols denote earlier (later) times. The $p_\mathrm{M} = 0.58$ line (dashed) is shown for comparison.

Thus, the principal finding of an evolution along the $p_\mathrm{M} \approx 1/2$ line with increasing q_M toward the $\beta = 0$ line, which is shortly before it reaches the $p_\mathrm{M} = 2(1 - q_\mathrm{M})$ equilibrium line, is recovered over a range of different circumstances, but the quality of convergence depends on how well we can approach the high magnetic Reynolds number limit.

V. CONCLUSIONS

Our work has demonstrated that the decay of turbulence with kinetic helicity leads to a nonconventional intermediate magnetic decay law with $p_\mathrm{M} \approx 1/2$ and q_M slowly increasing from about 0.4 to 0.6 before both p_M and q_M are expected to approach 2/3. Qualitatively, our results are easily explained. At early times, a bihelical magnetic helicity spectrum develops and it grows until it reaches equipartition at the wave number where the magnetic spectrum peaks. At small scales, the sign of the magnetic helicity agrees with that of the kinetic helicity. At early times, however, no net magnetic helicity can be produced. Therefore, magnetic field with negative helicity is generated simultaneously at larger scales. This can also be understood as a result of mean-field dynamo theory, where the sign of magnetic helicity at large scales agrees with the sign of α_dyn which, in turn, is a negative multiple of the kinetic helicity [1,2].

At later times, the magnetic helicity at small scales gets dissipated resistivity, so that part of the magnetic helicity spectrum is gradually lost until the entire magnetic helicity spectrum has the same sign (negative) at all k. The kinetic helicity has then also reversed sign, but it is very small

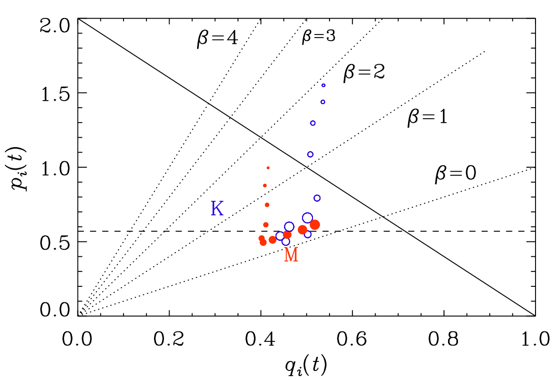

FIG. 14. *pq* diagram with constant $\nu = \eta = 10^{-6}$ for $\mathrm{Pr_M} = 1$. Again, smaller (larger) symbols denote earlier (later) times and the $p_\mathrm{M} = 0.58$ line (dashed) is shown for comparison.

and sustained only by the current helicity. After that time, the magnetic energy spectrum shows an inverse cascade during which $\langle \boldsymbol{B}^2 \rangle \xi_{\mathrm{M}}^{1+\beta_{\mathrm{M}}} \approx$ const with $\beta_{\mathrm{M}} \to 0$; see Eq. (15).

These new insights affect our understanding of all cases of decaying turbulence with initial kinetic helicity in electrically conducting media, such as plasma and liquid metal experiments, specifically the braked torus experiment, neutron stars, galaxy clusters, inertial fusion confinement plasmas, and the early universe. Thus, we predict that experiments should approach an evolutionary track in the pq diagram close to the $p_{\mathrm{M}} \approx 1/2$ line for many tens of thousands of turnover times if Re_{M} is large enough. Regarding applications to the early universe, the evolution in the $\langle \boldsymbol{B}^2 \rangle - \xi_{\mathrm{M}}$ diagram (see Fig. 11 of Ref. [32]) will be slightly steeper than for an initially fully helical magnetic field. This is because β_{M} is already close to zero.

We recall that kinetic and two-fluid effects have been neglected in the present work. While this should be appropriate for liquid metal experiments and the early universe, it may not be accurate for plasma experiments and galaxy clusters. Even in the dense neutron stars, Hall drift may play a role [49]. At present, not much is known about the importance of kinetic and two-fluid effects for plasma decay in the presence of helicity, so there is still a lot of room for basic studies in the field.

The new evolutionary phase of decaying magnetic fields with initial kinetic helicity follows after an early phase of an exponential increase of the magnetic energy by dynamo action. It is here that such a process has been simulated. To be able to achieve this, it was necessary to reach rather large values of Re_{M}. The subsequent decay phase with $p_{\mathrm{M}} \approx 1/2$ has so far only been seen in the decaying phase of such a dynamo process. During that time, the magnetic energy is already decaying, but the system clearly captures signatures of the initial kinetic helicity in the system, which then, at later times, disappears in favor of producing first current helicity and later magnetic helicity.

The phenomenon of magnetic field amplification at intermediate times is a phenomenon specific to high magnetic Reynolds numbers, which are only now becoming accessible to simulations. At present, no detailed comparison with dynamo decay experiments is possible yet, because no time dependence of the magnetic field has been obtained. The best such experiment is that of two laser beams producing colliding plasma jets directed toward each other, leading to magnetic field generation that can be monitored through Faraday rotation measurements [29]. The situation is complicated further by the fact that in the experiments performed so far, the buildup phase of the turbulence constitutes a significant fraction of the total time available. One might therefore want to consider a model for the buildup of the turbulence as well, which has not yet been attempted.

ACKNOWLEDGMENTS

We thank Eric Blackman and two anonymous referees for useful comments. A.B. acknowledges the University of Colorado's support through the George Ellery Hale visiting faculty appointment. T.K. acknowledges the High Energy and Cosmology Division and Associate Membership Program at International Center for Theoretical Physics (Trieste, Italy) for hospitality and partial support. We also thank Nordita for hospitality during the programs on Cosmological Magnetic Fields in 2015 (A.B., T.K., A.G.T., T.V.) and on Chiral Magnetic Phenomena in 2018 (A.B., T.K., S.M., A.R.P., T.V.). Support through the NSF Astrophysics and Astronomy Grant (AAG) Program (Grants No. AST1615940 and No. AST1615100), the Research Council of Norway (FRINATEK Grant No. 231444), the Swiss NSF SCOPES (Grant No. IZ7370-152581), and the Georgian Shota Rustaveli NSF (Grant No. FR/264/6-350/14) are gratefully acknowledged. T.V. is supported by the U.S. Department of Energy, Office of High Energy Physics, under Award No. DE-SC0018330 at Arizona State University. We acknowledge the allocation of computing resources provided by the Swedish National Allocations Committee at the Center for Parallel Computers at the Royal Institute of Technology in Stockholm. This work utilized the Janus supercomputer, which is supported by the National Science Foundation (Award No. CNS-0821794), the University of Colorado Boulder, the University of Colorado Denver, and the National Center for Atmospheric Research. The Janus supercomputer is operated by the University of Colorado Boulder.

[1] H. K. Moffatt, *Magnetic Field Generation in Electrically Conducting Fluids* (Cambridge University Press, Cambridge, UK, 1978).

[2] F. Krause and K.-H. Rädler, *Mean-Field Magnetohydrodynamics and Dynamo Theory* (Pergamon Press, Oxford, UK, 1980).

[3] A. Gailitis, O. Lielausis, S. Dementév, E. Platacis, A. Cifersons, G. Gerbeth, T. Gundrum, F. Stefani, M. Christen, H. Hänel, and G. Will, Detection of a Flow Induced Magnetic Field Eigenmode in the Riga Dynamo Facility, Phys. Rev. Lett. **84**, 4365 (2000).

[4] A. Gailitis, O. Lielausis, E. Platacis, S. Dement'ev, A. Cifersons, G. Gerbeth, T. Gundrum, F. Stefani, M. Christen, and G. Will, Magnetic Field Saturation in the Riga Dynamo Experiment, Phys. Rev. Lett. **86**, 3024 (2001).

[5] R. Stieglitz and U. Müller, Experimental demonstration of a homogeneous two-scale dynamo, Phys. Fluids **13**, 561 (2001).

[6] K.-H. Rädler, M. Rheinhardt, E. Apstein, and H. Fuchs, On the mean-field theory of the Karlsruhe dynamo experiment I. Kinematic theory, Magnetohydrodynamics **38**, 41 (2002).

[7] R. Monchaux, M. Berhanu, M. Bourgoin, M. Moulin, P. Odier, J.-F. Pinton *et al.*, Generation of Magnetic Field by Dynamo Action in a Turbulent Flow of Liquid Sodium, Phys. Rev. Lett. **98**, 044502 (2007).

[8] M. Berhanu, R. Monchaux, S. Fauve, N. Mordant, F. Pétrélis, A. Chiffaudel, F. Daviaud, B. Dubrulle, L. Marié, F. Ravelet, M. Bourgoin, P. Odier, J.-F. Pinton, and R. Volk, Magnetic field reversals in an experimental turbulent dynamo, Europhys. Lett. **77**, 59001 (2007).

[9] D. P. Lathrop, W. L. Shew, and D. R. Sisan, Laboratory experiments on the transition to MHD dynamos, Plasmas Phys. Contr. Fusion **43**, A151 (2001).

[10] D. S. Zimmerman, S. A. Triana, H.-C. Nataf, and D. P. Lathrop, A turbulent, high magnetic Reynolds number experimental model of Earth's core, J. Geophys. Res. **119**, 4538 (2014).

[11] E. J. Spence, K. Reuter, and C. B. Forest, A spherical plasma dynamo experiment, Astrophys. J. **700**, 470 (2009).

[12] C. M. Cooper, J. Wallace, M. Brookhart, M. Clark, C. Collins, W. X. Ding, K. Flanagan, I. Khalzov, Y. Li, J. Milhone *et al.*, The Madison plasma dynamo experiment: A facility for studying laboratory plasma astrophysics, Phys. Plasmas **21**, 013505 (2014).

[13] P. Frick, V. Noskov, S. Denisov, S. Khripchenko, D. Sokoloff, R. Stepanov, and A. Sukhanovsky, Non-stationary screw flow in a toroidal channel: Way to a laboratory dynamo experiment, Magnetohydrodynamics **38**, 143 (2002).

[14] V. Noskov, S. Denisov, R. Stepanov, and P. Frick, Turbulent viscosity and turbulent magnetic diffusivity in a decaying spin-down flow of liquid sodium, Phys. Rev. E **85**, 016303 (2012).

[15] P. Frick and I. Mizeva, MHD Turbulence in spin-down flows of liquid metals, arXiv:1709.08333.

[16] W. Dobler, P. Frick, and R. Stepanov, The screw dynamo in a time-dependent pipe flow, Phys. Rev. E **67**, 056309 (2003).

[17] R. C. Duncan and C. Thompson, Formation of very strongly magnetized neutron stars: Implications for γ-ray bursts, Astrophys. J. **392**, L9 (1992).

[18] C. Thompson and R. C. Duncan, A model of the tidal interaction between M81 and NGC3077, Astrophys. J. **408**, 194 (1993).

[19] K. Kajantie and H. Kurki-Suonio, Bubble growth and droplet decay in the quark-hadron phase transition in the early universe, Phys. Rev. D **34**, 1719 (1986).

[20] M. S. Turner, E. J. Weinberg, and L. M. Widrow, Bubble nucleation in first-order inflation and other cosmological phase transitions, Phys. Rev. D **46**, 2384 (1992).

[21] M. S. Turner and L. M. Widrow, Inflation produced, large scale magnetic fields, Phys. Rev. D **37**, 2743 (1988).

[22] B. Ratra, Cosmological "seed" magnetic field from inflation, Astrophys. J. **391**, L1 (1992).

[23] K. Roettiger, J. O. Burns, and J. M. Stone, A cluster merger and the origin of the extended radio emission in Abell 3667, Astrophys. J. **518**, 603 (1999).

[24] K. Roettiger, J. M. Stone, and J. O. Burns, Magnetic field evolution in merging clusters of galaxies, Astrophys. J. **518**, 594 (1999).

[25] S. S. R. Offner, R. I. Klein, and C. F. McKee, Driven and decaying turbulence simulations of low-mass star formation: From clumps to cores to protostars, Astrophys. J. **686**, 1174 (2008).
[26] J. Guillochon and M. McCourt, Simulations of magnetic fields in tidally disrupted stars, Astrophys. J. **834**, L19 (2017).
[27] C. K. Li, P. Tzeferacos, D. Lamb, G. Gregori, P. A. Norreys, M. J. Rosenberg, R. K. Follett, D. H. Froula, M. Koenig, F. H. Seguin *et al.*, Scaled laboratory experiments explain the kink behaviour of the Crab Nebula jet, Nat. Commun. **7**, 13081 (2016).
[28] P. Tzeferacos, A. Rigby, A. Bott, A. R. Bell, R. Bingham, A. Casner, F. Cattaneo, E. M. Churazov, J. Emig, N. Flocke *et al.*, Numerical modeling of laser-driven experiments aiming to demonstrate magnetic field amplification via turbulent dynamo, Phys. Plasmas **24**, 041404 (2017).
[29] P. Tzeferacos, A. Rigby, A. F. A. Bott, A. R. Bell, R. Bingham, A. Casner, F. Cattaneo, E. M. Churazov, J. Emig, F. Fiuza *et al.*, Laboratory evidence of dynamo amplification of magnetic fields in a turbulent plasma, Nat. Commun. **9**, 591 (2018).
[30] E. G. Blackman, Bihelical magnetic relaxation and large scale magnetic field growth, Phys. Plasmas **12**, 012304 (2005).
[31] K. Park, On the inverse transfer of (non-)helical magnetic energy in a decaying magnetohydrodynamic turbulence, Month. Not. Roy. Astron. Soc. **472**, 1628 (2017).
[32] A. Brandenburg, T. Kahniashvili, S. Mandal, A. Roper Pol, A. G. Tevzadze, and T. Vachaspati, Evolution of hydromagnetic turbulence from the electroweak phase transition, Phys. Rev. D **96**, 123528 (2017).
[33] E. G. Blackman and A. Brandenburg, Dynamic nonlinearity in large scale dynamos with shear, Astrophys. J. **579**, 359 (2002).
[34] A. Brandenburg, The inverse cascade and nonlinear α-effect in simulations of isotropic helical hydromagnetic turbulence, Astrophys. J. **550**, 824 (2001).
[35] G. K. Batchelor and I. Proudman, The large-scale structure of homogeneous turbulence, Phil. Trans. Roy. Soc., A **248**, 369 (1956).
[36] P. G. Saffman, Note on decay of homogeneous turbulence, Phys. Fluids **10**, 1349 (1967).
[37] A. Brandenburg and T. Kahniashvili, Classes of Hydrodynamic and Magnetohydrodynamic Turbulent Decay, Phys. Rev. Lett. **118**, 055102 (2017).
[38] K. Subramanian, The origin, evolution and signatures of primordial magnetic fields, Rep. Prog. Phys. **79**, 076901 (2016).
[39] A. S. Monin and A. M. Yaglom, *Statistical Fluid Mechanics, Mechanics of Turbulence*, Vol. 2 (MIT Press, Cambridge, MA, 1971).
[40] R. Durrer and C. Caprini, Primordial magnetic fields and causality, J. Cosmol. Astropart. Phys. **11**, 010 (2003).
[41] P. Olesen, Inverse cascades and primordial magnetic fields, Phys. Lett. B **398**, 321 (1997).
[42] P. Olesen, Dimensional reduction in freely decaying turbulent non-helical magnetic fields, arXiv:1509.08962.
[43] D. Biskamp and W.-C. Müller, Decay Laws for Three-Dimensional Magnetohydrodynamic Turbulence, Phys. Rev. Lett. **83**, 2195 (1999).
[44] A. Brandenburg, Pencil Code, version v2018.12.16 (2018), doi: 10.5281/zenodo.2315093, https://github.com/pencil-code.
[45] A. Brandenburg, T. Kahniashvili, and A. G. Tevzadze, Nonhelical Inverse Transfer of a Decaying Turbulent Magnetic Field, Phys. Rev. Lett. **114**, 075001 (2015).
[46] T. Kahniashvili, A. G. Tevzadze, A. Brandenburg, and A. Neronov, Evolution of primordial magnetic fields from phase transitions, Phys. Rev. D **87**, 083007 (2013).
[47] A. Berera and M. Linkmann, Magnetic helicity and the evolution of decaying magnetohydrodynamic turbulence, Phys. Rev. E **90**, 041003(R) (2014).
[48] A. Pouquet, U. Frisch, and J. Léorat, Strong MHD helical turbulence and the nonlinear dynamo effect, J. Fluid Mech. **77**, 321 (1976).
[49] M. Rheinhardt and U. Geppert, Hall-Drift-Induced Magnetic Field Instability in Neutron Stars, Phys. Rev. Lett. **88**, 101103 (2002).